HHS Public Access

Author manuscript

Gut. Author manuscript; available in PMC 2024 April 01.

Published in final edited form as:

Gut. 2023 April ; 72(4): 736–748. doi:10.1136/gutjnl-2021-326514.

Novel microenvironment-based classification of intrahepatic cholangiocarcinoma with therapeutic implications

Miguel A Martin-Serrano[1], **Benjamin Kepecs**[2], **Miguel Torres-Martin**[3], **Emily R Bramel**[1,4], **Philipp K Haber**[1], **Elliot Merritt**[2,5], **Alexander Rialdi**[1,6], **Nesteene Joy Param**[4,6], **Miho Maeda**[1], **Katherine E Lindblad**[1,4,5,6], **James K Carter**[1,4], **Marina Barcena-Varela**[1,5,6], **Vincenzo Mazzaferro**[7], **Myron Schwartz**[8], **Silvia Affo**[9], **Robert F Schwabe**[10], **Augusto Villanueva**[1], **Ernesto Guccione**[1,6], **Scott L Friedman**[1], **Amaia Lujambio**[1,4,5,6], **Anna Tocheva**[2,5], **Josep M Llovet**[1,3,11], **Swan N Thung**[12], **Alexander M Tsankov**[2], **Daniela Sia**[1]

[1]Division of Liver Diseases, Department of Medicine, Tisch Cancer Institute, Liver Cancer Program, Icahn School of Medicine at Mount Sinai, New York, New York, USA

[2]Department of Genetics and Genomic Sciences, Icahn School of Medicine at Mount Sinai, New York, New York, USA

[3]Translational Research in Hepatic Oncology, Liver Unit, IDIBAPS, Hospital Clinic, University of Barcelona, Barcelona, Catalunya, Spain

[4]Graduate School of Biomedical Sciences, Icahn School of Medicine at Mount Sinai, New York, New York, USA

[5]The Precision Immunology Institute (PrIISM), Icahn School of Medicine at Mount Sinai, New York, New York, USA

Correspondence to Dr Daniela Sia, Division of Liver Diseases, Department of Medicine, Tisch Cancer Institute, Liver Cancer Program, Icahn School of Medicine at Mount Sinai, New York, New York, USA; daniela.sia@mssm.edu.
BK and MT-M contributed equally.

Contributors DS designed the research, obtained funding and acts as guarantor for the overall content; MAM-S, MM, ST, MB-V, KL, NJP and EB performed the experiments. MAM-S, MM, JC and EB performed immunohistochemical analysis. DS, AV, BK, MT-M and PH conducted the in silico analyses. EM, AR, EG and AT performed coculture experiments. SA, RS and AL provided plasmids and advised on the murine models. VM, MS, SLF and JL collected the tissues and clinical data. BK performed scRNA-seq and ligand bulk RNA-seq correlation analyses designed by AMT, DS, MAM-S, BK and AMT, interpreted the results. DS, MAM-S, BK and AMT, interpreted the results. DS wrote the manuscript. All authors reviewed, edited and approved the manuscript.

Competing interests JML is receiving research support from Bayer HealthCare Pharmaceuticals, Eisai Inc, Bristol-Myers Squibb, Boehringer-Ingelheim and Ipsen, and consulting fees from Eli Lilly, Bayer HealthCare Pharmaceuticals, Bristol-Myers Squibb, Eisai Inc, Celsion Corporation, Exelixis, Merck, Ipsen, Genentech, Roche, Glycotest, Nucleix, Sirtex, Mina Alpha Ltd and AstraZeneca. AV has received consulting fees from Genentech, Guidepoint, Fujifilm, Boehringer Ingelheim, FirstWord, and MHLife Sciences; advisory board fees from Exact Sciences, Nucleix, Gilead and NGM Pharmaceuticals; and research support from Eisai.

Patient and public involvement Patients and/or the public were not involved in the design, or conduct, or reporting, or dissemination plans of this research.

Patient consent for publication Not applicable.

Provenance and peer review Not commissioned; externally peer reviewed.

[6]Department of Oncological Sciences, Tisch Cancer Institute, Icahn School of Medicine at Mount Sinai, New York, New York, USA

[7]General Surgery and Liver Transplantation Unit, Department of Oncology and Hemato-Oncology, University of Milan and Istituto Nazionale Tumori, IRCCS Foundation, Milano, Lombardia, Italy

[8]Department of Surgery, Tisch Cancer Institute, Liver Cancer Program, Icahn School of Medicine at Mount Sinai, New York, New York, USA

[9]Institut d'Investigacions Biomèdiques August Pi i Sunyer (IDIBAPS), Barcelona, Catalunya, Spain

[10]Department of Medicine, Columbia University, New York, New York, USA

[11]Institució Catalana de Recerca i Estudis Avançats, Barcelona, Spain

[12]Department of Pathology, Liver Cancer Program, Icahn School of Medicine at Mount Sinai, New York, New York, USA

Abstract

Objective—The diversity of the tumour microenvironment (TME) of intrahepatic cholangiocarcinoma (iCCA) has not been comprehensively assessed. We aimed to generate a novel molecular iCCA classifier that incorporates elements of the stroma, tumour and immune microenvironment ('STIM' classification).

Design—We applied virtual deconvolution to transcriptomic data from ~900 iCCAs, enabling us to devise a novel classification by selecting for the most relevant TME components. Murine models were generated through hydrodynamic tail vein injection and compared with the human disease.

Results—iCCA is composed of five robust STIM classes encompassing both inflamed (35%) and non-inflamed profiles (65%). The inflamed classes, named *immune classical* (~10%) and *inflammatory stroma* (~25%), differ in oncogenic pathways and extent of desmoplasia, with the *inflammatory stroma* showing T cell exhaustion, abundant stroma and *KRAS* mutations ($p<0.001$). Analysis of cell–cell interactions highlights cancer-associated fibroblast subtypes as potential mediators of immune evasion. Among the non-inflamed classes, the *desert-like class* (~20%) harbours the lowest immune infiltration with abundant regulatory T cells ($p<0.001$), whereas the *hepatic stem-like* class (~35%) is enriched in 'M2-like' macrophages, mutations in *IDH1/2* and *BAP1,* and *FGFR2* fusions. The remaining class (*tumour classical*: ~10%) is defined by cell cycle pathways and poor prognosis. Comparative analysis unveils high similarity between a *KRAS/p19* murine model and the *inflammatory stroma* class ($p=0.02$). The KRAS-SOS inhibitor, BI3406, sensitises a *KRAS*-mutant iCCA murine model to anti-PD1 therapy.

Conclusions—We describe a comprehensive TME-based stratification of iCCA. Cross-species analysis establishes murine models that align closely to human iCCA for the preclinical testing of combination strategies.

INTRODUCTION

Intrahepatic cholangiocarcinoma (iCCA) is a poorly understood biliary malignancy.[1] The incidence of iCCA has been steadily increasing over the past 40 years,[2] while its prognosis has remained dismal.[1] Despite recent breakthroughs have led to the FDA approval of FGFR and IDH1 inhibitors,[3–5] the 5-year survival rate remains less than 10%.[1]

Immunotherapy with checkpoint inhibitors (ICIs) and related strategies targeting the tumour microenvironment (TME) have conferred impressive survival benefits in many solid cancers.[6] While data in iCCA are limited, initial clinical results have been disappointing.[7] Thus, to move forward, strategies combining targeted therapies and immunotherapies will likely be required. Before doing so, a deeper analysis of the TME composition and its relationship with the molecular subtypes of iCCA is essential to stratify patient populations for precision therapies.

Previous studies had begun to establish iCCA classifications[8–10] using available methods but did not faithfully assess the complexity of the TME. To date, only one study has analysed the immune landscape of iCCA and described the existence of four immune subtypes.[11] Unfortunately, this classification did not correlate with key molecular aberrations (ie, mutations, chromosomal aberrations, etc) or previously described iCCA molecular subtypes,[8–10] greatly limiting its utility for the rational design of combination therapies targeting both the tumour and its microenvironment.

Herein, using state-of-the-art methodology, we have elucidated the genotype–immunophenotype relationships and provided a novel comprehensive classification of iCCA (called stroma, tumour, immune microenvironment based or STIM) that establishes a robust platform for disease stratification. Furthermore, cross-species analysis with the most commonly used murine iCCA models[12–15] reinforces their value for translational studies.

MATERIALS AND METHODS

Human cohorts

A total of 961 samples were obtained from seven public datasets[8 9 11 16–19] (online supplemental table S1). The ICGC JAPAN dataset[16] was used as training cohort. The other six datasets (DENMARK,[8] ICGC SINGAPORE,[17] MT SINAI,[9] TCGA-CHOL,[18] FRANCE[11] and Fu-CHINA)[19] were used as validation (online supplemental figure S1). Patients or the public were not involved in the design, or conduct, or reporting, or dissemination plans of our research.

Virtual deconstruction and STIM classification

We performed gene expression deconvolution of the training cohort[16] using the non-negative matrix factorisation (NMF) method[20] using default settings and 10 as number of factors to retrieve the most robust context-dependent expression patterns (online supplemental figure S2). In the NMF method, each gene is assigned a weight; those genes with the highest weight for a specific pattern of gene expression would represent the *exemplar genes* of that pattern (online supplemental table S2). Next, we characterised each expression pattern

using transcriptomic tools (ie, David, EnrichR) to ultimately associate the *exemplar genes* to specific gene expression profiles. We then devised a novel classification, called STIM, from an unsupervised analysis using the NMF-consensus module after selecting for the most relevant microenvironment-related patterns (online supplemental figure S1 and S2). Genes overexpressed in each STIM class were identified using DESeq2 (padj <0.05, online supplemental table S3). The five STIM classes were then molecularly characterised using previously published signatures and Molecular Signature Database gene sets (MSigDB, www.broadinstitute.org/msigdb (online supplemental table S4). The STIM classifier was generated using the top 100 differentially expressed genes in each STIM class (padj <0.001) in the training set (online supplemental table S5). The signature was tested in the validation datasets using nearest template prediction.[21]

Statistical analysis

Correlations between molecular classes and other variables were analysed by Fisher's exact test and Wilcoxon rank-sum test for categorical and continuous data, respectively.

For more information, see online supplemental methods.

RESULTS

Virtual deconstruction of the TME identifies five novel iCCA classes

The clinical and molecular features of a tumour are dictated by the tumorous cells as well as other TME components, including fibroblasts, immune cells and the extracellular matrix (ECM). In order to extract all possible sources of non-tumoural transcriptomic signals, we performed an unsupervised clustering of 122 iCCAs[16] using only the *exemplar genes* of the most relevant TME-dependent elements. The analysis identified five STIM classes.

Overall, we identified both inflamed and non-inflamed classes with the latter accounting for ~65% of the cohort (figure 1A). The two inflamed classes, hereafter termed *immune classical* and *inflammatory stroma,* were dominated by an immune and stromal component. In particular, while both classes could be classified as inflamed due to the relatively high presence of actual immune infiltration (p<0.05 for all, figure 1B), the *inflammatory stroma* showed abundance of desmoplastic reaction (p=0.005, figure 1C,D) along with signatures suggestive of ECM deposition,[22] high stiffness[23] (all p<0.01) and an activated inflammatory stroma[24] (19% vs 68%, p=0.002, figure 1A).

The remaining STIM classes resembled 'cold tumours' as indicated by the lower immune enrichment score (p<0.001), with the *desert-like* class (~20%) showing the lowest (p<0.001, figure 1A). The largest STIM class accounted for ~50% of the non-inflamed tumours and showed significant overlap (~90%) with the previously reported iCCA class with stem cell features,[10] and thus named *hepatic stem-like*. The last group of the non-inflamed iCCAs (~12%) was named *tumour classical* due to the high expression of cholangiocyte markers (figure 1A, p<0.01).

To validate the classification, we generated a STIM classifier and applied it to five independent datasets. Nearly all samples were confidently assigned (FDR <0.05) to one of

the five STIM classes; more importantly, the main features of each class were successfully reproduced, confirming robustness of our classification (figure 1E–F, online supplemental figure S3).

Overall, we have identified five robust iCCA classes with different immune, tumour and stromal composition. Our data suggest that the majority of iCCAs resemble cold tumours, while the inflamed classes differ significantly in their desmoplastic features.

The STIM classes reflect distinct immune composition

Next, we assessed the actual immune composition across the STIM classes using CIBERSORTx. The analysis suggested a higher presence of $CD8^+$ T cells ($p<0.001$) and gamma delta T cells ($p<0.01$) in the inflamed classes, while regulatory T cells (Tregs) were more abundant in the *desert-like* class ($p<0.001$ and $p=0.03$ vs others, figure 2A–B). Finally, M2-like macrophages were higher in the *hepatic stem-like* class ($p<0.001$ vs others). MCP counter yielded a similar immune composition (online supplemental figure S4A). Immunostaining for CD8a (~32% in inflamed vs 16% in non-inflamed classes, $p=0.07$, figure 2C, online supplemental figure S4B) and FOXP3 (60% in the *desert-like* class vs 34% in others, p=n.s., figure 2D) confirmed the deconvolution results, although no significance was reached probably due to the small sample size. Expression of the human leucocyte antigen molecules was significantly lower in the *desert-like* class, whereas immune checkpoint molecules were overall higher expressed in the inflamed classes ($p<0.05$ vs non-inflamed, online supplemental figure S4C,D), although protein positivity for PD-L1 or PD1 was overall low (6% and 8%, respectively online supplemental figure S4E). Finally, we used a public single-cell RNA-sequencing (scRNA-seq) iCCA dataset[25] to derive signatures specific for the main TME cell types (online supplemental table S6). Deconvolution using iCCA-specific signatures confirmed our results (online supplemental figure S5). We also converted the scRNA-seq of four naïve-treatment iCCAs from this scRNA-seq study[25] into pseudo-bulk and applied our STIM classifier. Sample 24T2 was assigned to the *inflammatory stroma class*, while the others were each assigned to the non-inflamed classes (online supplemental figure S6A). Consistent with our classification, sample 24T2 showed the lowest tumour purity and the largest fraction of T/NK and CAF cells.

We next sought to compare our STIM classes with other TME classifications (figure 2E). Overall, previously described classes of iCCA,[11] eCCA[26] and HCC[27 28] enriched in stromal components overlapped with our *inflammatory stroma,* including the previously described I2 and I4 subtypes of iCCA,[11] which capture immunogenic tumours characterised by immune response as well as abundant fibroblasts (figure 2E). Similarly, the inflamed subtypes of HCC overlapped with the inflamed classes of iCCA with the immune exhausted HCC class[27 28] characterised by stromal deposition, TGFB signalling and T cell exhaustion being enriched in our *inflammatory stroma*, while the immune active of HCC[27 28] was enriched in our *immune classical*. No overlap was observed between the immune class of eCCA and those of iCCA or HCC. Among the stem-like classes of HCC, only the EPCAM +gene signature of HCC[29] was enriched in our *hepatic stem-like* class (23% vs 7%, $p=0.0001$, figure 2E).

Our findings suggest that the immune composition differs across the STIM classes, with the inflamed classes showing abundance of $CD8^+$ and CAFs, and the non-inflamed classes presenting distinct immunosuppressive programmes.

Single-cell characterisation of cancer-associated fibroblasts

To explore whether the intratumoural stroma may contribute to shape the TME and responses to ICIs, we next analysed the CAF subtypes in iCCA. In a recent scRNA-seq based study of iCCA,[25] five distinct CAF classes have been identified, including vascular CAF (vCAF), myofibroblastic CAF (mCAF), inflammatory CAF (iCAF), antigen-presenting CAF (apCAF) and epithelial CAF (eCAF).[25] After integrating the single-cell data across all patients from the mentioned scRNA-seq study,[25] we performed unsupervised clustering and de novo marker discovery (figure 3A,B) and generated signatures specific for each CAF subpopulation (online supplemental figure S6B), which closely matched the previously reported annotations.[25] We excluded eCAF-like cells since they could represent epithelial/CAF doublets; furthermore, we renamed iCAFs as imCAFs due to our observation that iCAFs and mCAFs were transcriptionally similar and the iCAFs represented an inflamed immunologically activated population of mCAFs rather than a distinct subtype. High concordance in CAF subtype markers was also observed between our myofibroblastic CAFs (both mCAFs and imCAFs) and the myCAFs recently identified in murine and human iCCAs.[15] Gene Ontology analysis supports different roles for the CAF subtypes (online supplemental table S7). Next, we measured the relative abundance of each CAF signature in bulk RNA-seq data. The imCAFs were abundant in both inflamed classes, while the mCAF subtype, which was characterised by high *POSTN* expression (figure 3B,D) and ECM signatures (online supplemental figure S6C), was found enriched in the *inflammatory stroma* ($p<0.01$, online supplemental figure S6D). This CAF subtype was strongly associated with a previously reported immunosuppressive transcriptional programme dependent on TGFβ signalling (malignant-ECM),[22] TGFβ signalling in the TME[30] and a signature of resistance to ICIs (IPRES,[31] figure 3E). Consistently, ligand–receptor interactions[32] between each CAF subpopulation and other cell types found that mCAFs displayed the strongest expression of *TGF*β ligands and the greatest number of *TGF*β interactions (online supplemental figure S6E–G).

The TGFβ pathway along with FGF and PFGF signaling has been associated with epithelial-mesenchymal transition (EMT).[33 34] Considering the emerging role played by EMT in immunosuppression[35] and its strong association with a signature of resistance to ICIs[31] ($p<0.001$, online supplemental figure S7A), we then focused on EMT-promoting interactions between CAFs and malignant cells.[36–39] We found TGFβ3–TGFBR2, PDGFC–PDGFRA, FGF7–FGFR1 and CXCL12–CXCR4 interactions with ligands predominantly expressed by CAFs (figure 3F). Overall, apCAFs seemed to promote EMT through CXCL12 interactions, imCAFs primarily through FGF interactions and mCAFs through TGFβ, while vCAFs were less involved. Each of these ligands was strongly associated with the EMT score in bulk RNA-seq data of iCCA confirming their association with this process and pinpointing potential additional mechanisms of resistance to ICIs (online supplemental figure S7).

Cell–cell interaction frequencies between CAFs and the other cell types unveiled a strong cross-talk between T/natural killer (NK) cells and imCAFs (figure 3G) that are highly abundant in the inflamed classes (online supplemental figure S6D). Focusing on unique cell–cell interactions in each subtype (figure 3H, online supplemental figure S8) linked imCAF-specific interactions *CCL5-ACKR4* and *CCL3-IDE* to immune response disruption, with the former interaction negatively regulating CCL5 signalling[40] and the latter degrading CCL3.[41] Of relevance, the inferred abundance of T and NK cells for each STIM sample showed high correlation with *CCL5* expression, suggesting that increased *CCL5* could be driving the immune infiltration, particularly in the inflamed *STIM* classes (figure 3I,J).

Overall, our results suggest that the stromal composition may play a critical role in shaping the TME of iCCA and potentially influencing immune responses to immunotherapy.

Mutational and structural aberrations differ across the STIM classes

We next characterised the mutational landscape of the STIM classes. To do so, we collected all samples with either WES or targeted-seq data available and correlated presence of mutations in driver genes with the STIM classes (figure 4A). Overall, *KRAS* mutations alone occurred more frequently in the *inflammatory stroma* (22% vs 8%, p=0.0006), whereas mutations in *BAP1* (28% vs 8%, p=0.00001) and *IDH1/2* genes (16% vs 7%, p=0.002 for *IDH1* and 7% vs 2%, p=0.02 for *IDH2*) as well as *FGFR2* fusions (13% vs 5%, p=0.005) were more frequent in the *hepatic stem-like* class. Finally, mutations in *TP53* alone were found enriched in the *tumour classical* (26% vs 15%, p=0.006) and *immune classical* classes (25% vs 14%, p=0.03). Co-occurrence of *TP53* and *KRAS* mutations was significantly more frequent in the *tumour classical* class (16% vs 4%, p=0.0003), whereas a non-significant trend was observed in the *desert-like* class compared with the rest (11% vs 5%, p=0.07). Interestingly, co-occurrence of *TP53* and *KRAS* mutations was significantly associated with presence of Tregs (online supplemental figure S9A–C); such enrichment was not observed in patients with mutations in *KRAS* or *TP53* alone.

Analysis of tumour mutational burden and neoantigen burden did not show a clear correlation between either parameter and the immune characteristics of the STIM classes (online supplemental figure S10), suggesting that other parameters may determine immunogenicity of this tumour type.

In terms of chromosomal instability, the *hepatic stem-like* and the *desert-like* classes showed a higher chromosomal load, mostly due to broad and focal losses (online supplemental figure S9D–G, online supplemental table S8). Among the more frequently deleted peaks in the *hepatic stem-like*, we identified loss of *SAV1* (chr14q22) and *VGLL4* (chr3p25.3), tumour suppressors of the Hippo pathway. Notably, *SAV1* expression correlated with its chromosomal loss[9] and a YAP1 signature (online supplemental figure S11A,B). Finally, 22% of tumours harboured at least one chromosomal deletion affecting an IFN-related gene; focal loss of chr16q24, involving genes such as *IRF8*, *IL4R* and *IL21R*, occurred more frequently in the *desert-like* class (p=0.02, online supplemental table S9).

Our data suggest that each class is characterised by specific mutations and structural alterations, which could contribute to shape the surrounding TME.

Targetable signalling pathways are altered in the STIM classes

We then investigated whether oncogenic pathways were differentially activated in the STIM classes (online supplemental tables S10–S14). As expected, inflammation-related pathways were enriched in the inflamed classes; metabolic-related pathways were significantly elevated in the *immune classical* whereas the *inflammatory stroma* was defined by several targetable oncogenic pathways (ie, KRAS, PI3K/AKT; figure 4B, online supplemental figure S11C,D). The *hepatic stem-like* class was enriched in stemness-related pathways (ie, NOTCH, YAP1, figure 4B). Finally, the *tumour classical* was enriched in cell cycle-related pathways, whereas the *desert-like* class was enriched in mitotic spindle. Interestingly, the WNT/β-catenin signalling was enriched in the *desert-like* class in the training dataset (figure 4B).

Overall, different pathways defined each STIM class with pathways previously associated with immune exclusion and immunoresistance being enriched in the non-inflamed classes (figure 4C).

Clinical correlates of the STIM classes

We then correlated the STIM classes with clinicopathological characteristics. In the MT SINAI cohort,[9] tumours of the *inflammatory stroma* class were more likely to present with advanced stage (p=0.02), perineural invasion (p=0.003) and invasion of the bile duct (p=0.03). Tumours of the *hepatic stem-like* were more likely HCV positive and at an early stage (p=0.04, online supplemental table S15). Tumours with small or large ducts were equally distributed, and 91% of iCCAs belonged to the mass-forming subtype; the remaining 9% showed a combined mass-forming and periductal infiltrating subtype, which was slightly enriched in the *immune classical* class (17% vs 5% in others, p=0.049).

Only few variables were available for the ICGC JAPAN[16] and SINGAPORE[17] cohorts which, unlike ours, comprised patients from both Western and Eastern countries with different aetiologies (ie, liver fluke). We confirmed early stage in patients of the *hepatic stem-like* class (stage I+II, 50% vs 20%, p=0.02) in the ICGC SINGAPORE dataset.[17] In this cohort, patients of the *hepatic stem-like* were more likely to be negative for liver flukes (93% negative vs 45% in others, p=0.0001). These associations were not confirmed in the Fu-CHINA cohort (online supplemental table S15) advising caution. In terms of outcome, the *tumour classical* had worse survival in the two ICGC datasets, whereas the *inflammatory stroma* was associated with poor survival in the ICGC JAPAN and FRANCE datasets (online supplemental figures S12 and S13). In multivariate analysis, the STIM classes were not consistently retained as independent predictors (online supplemental table S16).

Altogether, our results indicate that tumours of the *inflammatory stroma* and *tumour classical* classes are linked to more aggressive disease (ie, advanced stage), although they are not independent predictors of survival.

In vivo modelling of the STIM classes

Based on the growing reliance on preclinical models to define potential therapies, it was essential to determine whether commonly used iCCA mouse models recapitulate key

features of these human STIM classes. To do so, we interrogated four previously established murine models carrying either the frequently mutated driver gene *KRAS* in combination with loss of the tumour suppressor p19 (*KRAS/p19*[15] model) or dysregulation of signalling pathways known to play a crucial role in the molecular pathogenesis of iCCA including NOTCH, YAP1 and AKT1 (models used: *NICD1/AKT1*[12], *YAP1/AKT1*[13] and *FBXW7/AKT1*[14]). All murine models developed iCCA in our hands (figure 5A). Unsupervised clustering of RNA-seq data suggested higher similarity between tumours within each model (figure 5B). Prediction analysis using the STIM classifier revealed that the *KRAS/p19* model resembled the *inflammatory stroma*, while the other three mostly recapitulated the *hepatic stem-like* class (STIM classifier, FDR <0.05, figure 5C, first row). Consistently, pathways characteristic of the *inflammatory stroma* were enriched in the *KRAS/p19* tumours ($p<0.01$). However, protein secretion, NOTCH and YAP1 signalling, which are characteristic of the *hepatic stem-like*, were higher in the *NICD1/AKT1* and *YAP1/AKT1* models. Submap analysis, an unsupervised approach able to assess transcriptomic similarity between the whole transcriptome of different datasets, confirmed strong similarity between the *KRAS/p19* model and the *inflammatory stroma* class (figure 5D).

Finally, we analysed the immune composition of the murine tumours (figure 6A–G, online supplemental figures S14 and 15). We observed a significant enlargement of the myeloid compartment in all models compared with healthy livers, particularly granulocytic myeloid-derived suppressor cells (G-MDSCs). Interestingly, *KRAS/p19* tumours contained increased $CD8^+PD1^+$ T cells ($p=0.06$, online supplemental figure S16A–D). Accordingly, *KRAS*-mutant patients showed depletion of cytotoxic T cells and enrichment of myeloid cells (figure 6H). Finally, a robust and significant increase of the percentage of monocytic myeloid-derived suppressor cells and macrophages over the total $CD45^+$ cells was observed in the *YAP1/AKT1*. Consistently, human tumours with high YAP1 signature score showed a higher rate of macrophages (figure 6I, online supplemental figure S16E). Comparative analysis identified *PDGF-D*, which plays an important role in macrophage recruitment,[42] among the top overexpressed genes in both murine (figure 6J) and human YAP1-driven iCCAs (online supplemental table S17). To establish whether YAP1 activation could induce PDGF-D, we analysed transcriptomic data derived from isolated YAP1-positive liver cells collected at multiple time points on hepatocyte-specific YAP1 activation in doxycycline-inducible transgenic mice (*tetOYAP*, figure 1E in ref 43). This model is relevant since in the *YAP1/AKT1* model iCCA derives from the transformation of hepatocytes.[13] The analysis unveiled a gradual increase of *Pdgf-d* expression on YAP1 activation (figure 6K).

Overall, our data establish that the most commonly used murine models of iCCA recapitulate the largest STIM classes (*inflammatory stroma* and *hepatic stem like*), while comparative analysis identified YAP1 signalling as a potential mediator of macrophage recruitment.

In vivo drug testing of clinically relevant combination strategies

Tumours of the *inflammatory stroma* display abundance of immune cells, low T cell cytotoxicity and enrichment of the IPRES signature; based on this, we speculated that they are refractory to immunotherapy, and drugs targeting key immunosuppressive drivers

(ie, KRAS) may sensitise them to classical ICIs. To verify our hypothesis, we generated a syngeneic subcutaneous model by injecting KRAS-mutant cells (KAP) derived from the KRAS/p19 model. Once tumour reached a volume of 250 mm^3, mice were randomised to receive vehicle, the potent KRAS-SOS1 inhibitor BI-3406 with high selectivity for mutant *KRAS*,[44] anti-PD1 therapy or combination (figure 7A). All treatments were well tolerated (online supplemental figure S17). Only the combination significantly suppressed tumour growth (figure 7B) as further indicated by the tumour size at day 14 represented either as relative tumour volume (compared with baseline) or absolute measures in excised tumours on sacrifice (online supplemental figure S17B,C). Flow cytometry analysis of CD45 +cells (figure 7C–D) unveiled increase in proliferating $CD8^+$ T cells in the combination arm (p=0.07, CD8 +NK1.1+panel) and decrease of Tregs in both BI3406 and combination arms, although significance was not reached (figure 7C,D, Tregs panel). Single agents showed no impact on tumour growth confirming our hypothesis.

Tumours of the *hepatic stem-like* class are 'cold' with abundance of myeloid cells. While our data suggest an immunosuppressive role for YAP1 in these tumours, YAP1 inhibitors have not been successful due to toxicity. Tivozanib, a potent selective inhibitor of VEGFR1-3, is currently being tested as single agent and in combination with ICIs in cold tumours, including iCCA (NCT04645160, NCT05000294). To test if this combination could benefit cold iCCAs, we evaluated its efficacy in YAP1/AKT1 tumours (figure 7E). Interestingly, while tivozanib significantly suppressed tumour growth, the combination did not provide additional benefit (figure 7F–H). To confirm the translational validity of our *in vivo* results in a patient-relevant model of tumour/T cell interactions, we tested the same combinations in a co-culture system of iCCA patient-derived organoids (PDOs) (online supplemental figure S18A) and *in vitro* expanded autologous tumour-infiltrating lymphocytes (TILs) derived from one patient with heterozygous $KRAS^{G12D}$ mutation and one patient with wild-type *KRAS*. First, we demonstrated that the PDOs expressed high levels of MHC class I and upregulated PD-L1 following IFNg stimulation[45] (online supplemental figure S18B). Next, we determined the IC50 for both inhibitors and observed that both BI-3406 and tivozanib reduced the expression of PD-L1 but not MHCI following overnight stimulation with IFNg (online supplemental figure S18C,D). However, following 48-hour co-culture of PDO and TIL, only *KRAS* inhibition with BI-3406 synergised with PD-1 blockade to stimulate T cell activation as indicated by higher percentage of $CD8^+GZMB^+$ and $CD8^+CD25^+$ cells in the $KRAS^{G12D}$ mutant organoid (online supplemental figure S18E). Notably, tivozanib, anti-PD1 or combination had little or no impact on T cell activation supporting the lack of synergistic effect *in vivo* (online supplemental figure S18E).

Finally, when exploring in our mouse models the TOPAZ-1[46] combination of durvalumab (moAb anti-PD-L1) plus chemotherapy, we observed no differences between the chemotherapy plus ICI arm and the chemotherapy alone arm in terms of overall survival (figure 7I–J). The NICD/AKT1 model was chosen for this experiment based on the rationale that this combination regimen could 'turn cold tumours into hot' by inducing immunogenic cell death and ultimately facilitating an antitumour immune response.[47] Overall, murine tumours showed resistance to ICI and sensitivity to chemotherapy, while the combination strategy did not elicit any survival advantage (figure 7J). Weight loss was observed in mice

receiving chemotherapy (online supplemental figure S17E). In the TOPAZ-1 trial, objective response rates were 27% in the combo versus 19% in the gem/cis arm, ultimately suggesting that further investigation is needed to understand the immune and molecular mechanisms underpinning the observed responses and identify which patients may benefit from the addition of chemotherapy to ICIs.

Our data suggest that BI-3406 sensitise *KRAS*-mutant iCCAs to anti-PD1 therapy while tivozanib as single agent significantly suppresses tumour growth in YAP1-driven tumours although it fails to sensitise this type of cold tumours to PD1 therapy.

DISCUSSION

A thorough understanding of the TME's complexity is a significant unmet need to establish effective therapies in iCCA, as current treatments are largely ineffective. Through the virtual deconstruction of a large iCCA cohort, we have generated a new classification that unveils key actionable genotype–immunophenotype correlations and provides genomic evidence indicating that the immunogenicity of iCCA is partially influenced by the tumour genetic alterations (figure 4C).

Accumulating evidence from other solid tumours link responses to ICIs to baseline T cell infiltration[48 49] and the expression of immunosuppressive programmes.[22 48 50] Our analysis suggests that more than 60% of iCCAs harbour a non-inflamed phenotype with abundance of immunosuppressive elements. While the lack of tumour biopsies before or after treatment limit translation of these findings to clinical benefit, the results are in line with the poor responses observed thus far in iCCA patients receiving single agent anti-PD-1 therapy.[51] Among the non-inflamed classes, we have identified the *desert-like* which is defined by scarce immune infiltration, enrichment of Tregs and low expression of genes related to the antigen presenting machinery. Interestingly, the latter has been recently identified as the most relevant feature separating melanoma patients who respond or not to immunotherapy.[48]

The largest non-inflamed cluster, the *hepatic stem-like* (~35%), resembles the previously reported iCCA class with stem cell features.[10] Accordingly, this cluster showed enrichment of stemness-related pathways, *BAP1* and *IDH1* mutations. Alterations in *BAP1* and *IDH* genes have been associated with reduced T cell activity[52 53]; thus, studies are warranted to establish the rationale of combining IDH inhibitors with immunotherapy in iCCA. Focal deletion of *SAV1* occurred in ~30% of the *hepatic stem-like* class, suggesting that it may represent the main mechanism underlying YAP1 activation in these tumours. Evidence from other cancers suggest that YAP1 may induce immunosuppression through the recruitment of myeloid cells.[50] Notably, both YAP1-driven murine and human iCCAs resembled cold tumours with higher proportion of macrophages. Treatment of YAP1/AKT1 tumours with tivozanib suppressed tumour growth but failed to sensitise to anti-PD1 therapy. These results are relevant since tivozanib is currently being tested in combination with ICIs in cold tumours, including iCCA.

Mutations in driver genes, such as *KRAS* and *TP53,* may play a role in influencing the immune composition of several tumors.[50] In our analysis, co-occurrence of *TP53* and

KRAS mutations was associated with accumulation of Tregs and was more frequent in the non-inflamed classes, *desert-like* and *tumour classical*. The latter accounted for a small fraction of patients (~10%) and showed enrichment of cell cycle pathways. There is rationale for combining CDK inhibitors and ICIs[54]; whether this combination may provide benefit to these patients needs to be explored.

Baseline presence of T cells and IFN signalling has been associated with higher response rates to immunotherapy in melanoma. In iCCA, less than 35% of the cohort showed an inflamed phenotype and included the *immune classical* and *inflammatory stroma* classes. The *inflammatory stroma* was enriched in *KRAS* mutations and showed enrichment of elements (ie, mCAF subtype, TGFβ signalling) previously associated with innate resistance to ICIs in melanoma and lung.[55] Recent breakthroughs have led to the development of new potent KRAS inhibitors and the first clinical trials in combination with ICIs are ongoing in lung cancer, suggesting that similar strategies could benefit iCCA. Accordingly, *in vivo* treatment with BI-3406 sensitised *KRAS*-mutant iCCA to PD1 therapy through immunomodulatory mechanisms.

Our findings also underscore the potentially important role of CAFs in shaping the iCCA immune landscape. We observed a strong cross-talk between imCAFs and immune cells that could interfere with CCL5 recruitment or activation of T/NK cells. We also identified several EMT-related interactions between malignant cells and CAFs that could contribute to immunosuppression in otherwise inflamed tumours. *Ad hoc* functional studies are needed to validate the role of identified cell–cell interactions.

Our study provides key insights into the genotype–immunophenotype relationships of iCCA and pinpoints potential tumour-intrinsic and extrinsic mechanisms of immunosuppression and evasion. The successful *in vivo* modelling of the STIM classes within rodent models establishes a valuable platform to test combination strategies that is highly relevant and possibly more predictive of human treatment responses.

Supplementary Material

Refer to Web version on PubMed Central for supplementary material.

Acknowledgements

We would like to thank Professor Xin Chen for providing the pT3-EF5α-HA-FBXW7ΔF plasmid, Professor Lars Zender for providing the pCaggs-KRASG12D and pX330-sg-p19 plasmids, and Jill Gregory for her help with the design of figure 4C. We also would like to thank the Tisch Cancer Institute (TCI) Human Immune Monitoring Core (HIMC), the Flow Cytometry Shared Resource Facility, and the Biorepository and Pathology Core at Icahn School of Medicine at Mount Sinai.

Funding

This study was partially funded by the 2019 PhD Scientist Innovative Research Award and the Dr. Franklin Klion Young Scientist Award (DS), and the Cholangiocarcinoma Foundation (MAM-S). MAM-S is supported by the Margaret M. Brown Memorial Research Fellowship from the Cholangiocarcinoma Foundation. PH is supported by the fellowship grant of the German Research Foundation (DFG, HA 8754/1–1). JC is supported by grants from National Institutes of Health (T32GM007280 and T32GM062754). KL is supported by NIH T32 AI78892-12. MB-V is supported by the Asociación Española por el Estudio del Hígado (AEEH). SA is supported by a fellowship from ‘la Caixa’ Foundation (ID 100010434) and from the European Union’s Horizon 2020 research and innovation programme under the Marie Skłodowska-Curie grant agreement No 847648. AL is supported by Damon

Runyon-Rachleff Innovation Award (DR52-18), R37 Merit Award (R37CA230636), and Icahn School of Medicine at Mount Sinai. The Tisch Cancer Institute and related research facilities are supported by P30 CA196521. JML acknowledges his research funding from the Accelerator Award (HUNTER, Ref. C9380/A26813, partnership between the CRUK, AECC and AIRC), Samuel Waxman Cancer Research Foundation, Spanish National Health Institute (PID2019-105378RB-100), the Generalitat de Catalunya/AGAUR (SGR-1358). DS is supported by the Tisch Cancer Institute and Icahn School of Medicine at Mount Sinai. SLF is supported by the US Department of Defense (CA150272P3) and NIDDK (R01 DK56621 and R01 DK128289). AMT is supported by US Department of Defense (W81XWH2210079) and Icahn School of Medicine at Mount Sinai.

Data availability statement

Data are available in a public, open access repository. RNA-sequencing data generated in this study have been deposited in the GEO database (GSE171443). Previously published datasets analysed in this study are indicated in main Methods and detailed in online supplemental table 1.

REFERENCES

1. Banales JM, Marin JJG, Lamarca A, et al. Cholangiocarcinoma 2020: the next horizon in mechanisms and management. Nat Rev Gastroenterol Hepatol 2020;17:557–88. [PubMed: 32606456]
2. Khan SA, Tavolari S, Brandi G. Cholangiocarcinoma: epidemiology and risk factors. Liver Int 2019;39 Suppl 1:19–31. [PubMed: 30851228]
3. Abou-Alfa GK, Sahai V, Hollebecque A, et al. Pemigatinib for previously treated, locally advanced or metastatic cholangiocarcinoma: a multicentre, open-label, phase 2 study. Lancet Oncol 2020;21:671–84. [PubMed: 32203698]
4. Makawita S K Abou-Alfa G, Roychowdhury S, et al. Infigratinib in patients with advanced cholangiocarcinoma with *FGFR2* gene fusions/translocations: the PROOF 301 trial. Future Oncol 2020;16:2375–84. [PubMed: 32580579]
5. Abou-Alfa GK, Pandya SS, Zhu AX. Ivosidenib for advanced IDH1-mutant cholangiocarcinoma - Authors' reply. Lancet Oncol 2020;21:e371. [PubMed: 32758466]
6. Murciano-Goroff YR, Warner AB, Wolchok JD. The future of cancer immunotherapy: microenvironment-targeting combinations. Cell Res 2020;30:507–19. [PubMed: 32467593]
7. Loeuillard E, Conboy CB, Gores GJ, et al. Immunobiology of cholangiocarcinoma. JHEP Rep 2019;1:297–311. [PubMed: 32039381]
8. Andersen JB, Spee B, Blechacz BR, et al. Genomic and genetic characterization of cholangiocarcinoma identifies therapeutic targets for tyrosine kinase inhibitors. Gastroenterology 2012;142:1021–31. [PubMed: 22178589]
9. Sia D, Hoshida Y, Villanueva A, et al. Integrative molecular analysis of intrahepatic cholangiocarcinoma reveals 2 classes that have different outcomes. Gastroenterology 2013;144:829–40. [PubMed: 23295441]
10. Oishi N, Kumar MR, Roessler S, et al. Transcriptomic profiling reveals hepatic stem-like gene signatures and interplay of miR-200c and epithelial-mesenchymal transition in intrahepatic cholangiocarcinoma. Hepatology 2012;56:1792–803. [PubMed: 22707408]
11. Job S, Rapoud D, Dos Santos A, et al. Identification of four immune subtypes characterized by distinct composition and functions of tumor microenvironment in intrahepatic cholangiocarcinoma. Hepatology 2020;72:965–81. [PubMed: 31875970]
12. Fan B, Malato Y, Calvisi DF, et al. Cholangiocarcinomas can originate from hepatocytes in mice. J Clin Invest 2012;122:2911–5. [PubMed: 22797301]
13. Wang J, Dong M, Xu Z, et al. Notch2 controls hepatocyte-derived cholangiocarcinoma formation in mice. Oncogene 2018;37:3229–42. [PubMed: 29545603]
14. Wang J, Wang H, Peters M, et al. Loss of FBXW7 synergizes with activated Akt signaling to promote c-myc dependent cholangiocarcinogenesis. J Hepatol 2019;71:742–52. [PubMed: 31195063]

15. Affo S, Nair A, Brundu F, et al. Promotion of cholangiocarcinoma growth by diverse cancer-associated fibroblast subpopulations. Cancer Cell 2021;39:866–82. [PubMed: 33930309]
16. Nakamura H, Arai Y, Totoki Y, et al. Genomic spectra of biliary tract cancer. Nat Genet 2015;47:1003–10. [PubMed: 26258846]
17. Jusakul A, Cutcutache I, Yong CH, et al. Whole-Genome and epigenomic landscapes of etiologically distinct subtypes of cholangiocarcinoma. Cancer Discov 2017;7:1116–35. [PubMed: 28667006]
18. Farshidfar F, Zheng S, Gingras M-C, et al. Integrative genomic analysis of cholangiocarcinoma identifies distinct IDH-Mutant molecular profiles. Cell Rep 2017;19:2878–80. [PubMed: 28658632]
19. Dong L, Lu D, Chen R, et al. Proteogenomic characterization identifies clinically relevant subgroups of intrahepatic cholangiocarcinoma. Cancer Cell 2022;40:70–87. [PubMed: 34971568]
20. Brunet J-P, Tamayo P, Golub TR, et al. Metagenes and molecular pattern discovery using matrix factorization. Proc Natl Acad Sci U S A 2004;101:4164–9. [PubMed: 15016911]
21. Reich M, Liefeld T, Gould J, et al. GenePattern 2.0. Nat Genet 2006;38:500–1. [PubMed: 16642009]
22. Chakravarthy A, Khan L, Bensler NP, et al. TGF-β-associated extracellular matrix genes link cancer-associated fibroblasts to immune evasion and immunotherapy failure. Nat Commun 2018;9:4692. [PubMed: 30410077]
23. Pearce OMT, Delaine-Smith RM, Maniati E, et al. Deconstruction of a metastatic tumor microenvironment reveals a common matrix response in human cancers. Cancer Discov 2018;8:304–19. [PubMed: 29196464]
24. Moffitt RA, Marayati R, Flate EL, et al. Virtual microdissection identifies distinct tumor- and stroma-specific subtypes of pancreatic ductal adenocarcinoma. Nat Genet 2015;47:1168–78. [PubMed: 26343385]
25. Zhang M, Yang H, Wan L, et al. Single-Cell transcriptomic architecture and intercellular crosstalk of human intrahepatic cholangiocarcinoma. J Hepatol 2020;73:1118–30. [PubMed: 32505533]
26. Montal R, Sia D, Montironi C, et al. Molecular classification and therapeutic targets in extrahepatic cholangiocarcinoma. J Hepatol 2020;73:315–27. [PubMed: 32173382]
27. Montironi C, Castet F, Haber PK, et al. Inflamed and non-inflamed classes of HCC: a revised immunogenomic classification. Gut 2022. doi:10.1136/gutjnl-2021-325918. [Epub ahead of print: 23 Feb 2022].
28. Sia D, Jiao Y, Martinez-Quetglas I, et al. Identification of an Immune-specific class of hepatocellular carcinoma, based on molecular features. Gastroenterology 2017;153:812–26. [PubMed: 28624577]
29. Yamashita T, Ji J, Budhu A, et al. EpCAM-positive hepatocellular carcinoma cells are tumor-initiating cells with stem/progenitor cell features. Gastroenterology 2009;136:1012–24. [PubMed: 19150350]
30. Calon A, Lonardo E, Berenguer-Llergo A, et al. Stromal gene expression defines poor-prognosis subtypes in colorectal cancer. Nat Genet 2015;47:320–9. [PubMed: 25706628]
31. Hugo W, Zaretsky JM, Sun L, et al. Genomic and transcriptomic features of response to anti-PD-1 therapy in metastatic melanoma. Cell 2016;165:35–44. [PubMed: 26997480]
32. Vento-Tormo R, Efremova M, Botting RA, et al. Single-Cell reconstruction of the early maternal-fetal interface in humans. Nature 2018;563:347–53. [PubMed: 30429548]
33. Deshmukh AP, Vasaikar SV, Tomczak K, et al. Identification of EMT signaling cross-talk and gene regulatory networks by single-cell RNA sequencing. Proc Natl Acad Sci U S A 2021;118:e2102050118. [PubMed: 33941680]
34. Dongre A, Weinberg RA. New insights into the mechanisms of epithelial-mesenchymal transition and implications for cancer. Nat Rev Mol Cell Biol 2019;20:69–84. [PubMed: 30459476]
35. Taki M, Abiko K, Ukita M, et al. Tumor immune microenvironment during epithelial-mesenchymal transition. Clin Cancer Res 2021;27:4669–79. [PubMed: 33827891]
36. Jechlinger M, Sommer A, Moriggl R, et al. Autocrine PDGFR signaling promotes mammary cancer metastasis. J Clin Invest 2006;116:1561–70. [PubMed: 16741576]

37. Tomlinson DC, Baxter EW, Loadman PM, et al. FGFR1-induced epithelial to mesenchymal transition through MAPK/PLCγ/COX-2-mediated mechanisms. PLoS One 2012;7:e38972. [PubMed: 22701738]
38. Li L, Zhang S, Li H, et al. Fgfr3 promotes the growth and malignancy of melanoma by influencing EMT and the phosphorylation of ERK, Akt, and EGFR. BMC Cancer 2019;19:963. [PubMed: 31619201]
39. Lin Y, Ma Q, Li L, et al. The CXCL12-CXCR4 axis promotes migration, invasiveness, and EMT in human papillary thyroid carcinoma B-CPAP cells via NF-κB signaling. Biochem Cell Biol 2018;96:619–26. [PubMed: 29316404]
40. Matti C, Salnikov A, Artinger M, et al. ACKR4 recruits GRK3 prior to β-arrestins but can scavenge chemokines in the absence of β-arrestins. Front Immunol 2020;11:720. [PubMed: 32391018]
41. Ren M, Guo Q, Guo L, et al. Polymerization of MIP-1 chemokine (CCL3 and CCl4) and clearance of MIP-1 by insulin-degrading enzyme. Embo J 2010;29:3952–66. [PubMed: 20959807]
42. Uutela M, Wirzenius M, Paavonen K, et al. Pdgf-D induces macrophage recruitment, increased interstitial pressure, and blood vessel maturation during angiogenesis. Blood 2004;104:3198–204. [PubMed: 15271796]
43. Yimlamai D, Christodoulou C, Galli GG, et al. Hippo pathway activity influences liver cell fate. Cell 2014;157:1324–38. [PubMed: 24906150]
44. Hofmann MH, Gmachl M, Ramharter J, et al. BI-3406, a potent and selective SOS1-KRAS interaction inhibitor, is effective in KRas-driven cancers through combined MEK inhibition. Cancer Discov 2021;11:142–57. [PubMed: 32816843]
45. Dijkstra KK, Cattaneo CM, Weeber F, et al. Generation of Tumor-Reactive T cells by co-culture of peripheral blood lymphocytes and tumor organoids. Cell 2018;174:1586–98. [PubMed: 30100188]
46. DY O e.a.A.p.r., double-blind, placebo-controlled study of durvalumab in combination with gemcitabine plus cisplatin in patients with advanced biliary tract cancer: TOPAZ-1. 2022 ASCO Gastrointestinal Cancers Symposium Abstract 378.
47. Galluzzi L, Buqué A, Kepp O, et al. Immunological effects of conventional chemotherapy and targeted anticancer agents. Cancer Cell 2015;28:690–714. [PubMed: 26678337]
48. Grasso CS, Tsoi J, Onyshchenko M, et al. Conserved interferon-γ signaling drives clinical response to immune checkpoint blockade therapy in melanoma. Cancer Cell 2020;38:500–15. [PubMed: 32916126]
49. Herbst RS, Soria J-C, Kowanetz M, et al. Predictive correlates of response to the anti-PD-L1 antibody MPDL3280A in cancer patients. Nature 2014;515:563–7. [PubMed: 25428504]
50. Wellenstein MD, de Visser KE. Cancer-Cell-Intrinsic mechanisms shaping the tumor immune landscape. Immunity 2018;48:399–416. [PubMed: 29562192]
51. Piha-Paul SA, Oh D-Y, Ueno M, et al. Efficacy and safety of pembrolizumab for the treatment of advanced biliary cancer: results from the KEYNOTE-158 and KEYNOTE-028 studies. Int J Cancer 2020;147:2190–8. [PubMed: 32359091]
52. Figueiredo CR, Kalirai H, Sacco JJ, et al. Loss of BAP1 expression is associated with an immunosuppressive microenvironment in uveal melanoma, with implications for immunotherapy development. J Pathol 2020;250:420–39. [PubMed: 31960425]
53. Richardson LG, Choi BD, Curry WT. (R)-2-hydroxyglutarate drives immune quiescence in the tumor microenvironment of IDH-mutant gliomas. Transl Cancer Res 2019;8:S167–70. [PubMed: 30956952]
54. Zhang H, Christensen CL, Dries R, et al. Cdk7 inhibition potentiates genome instability triggering anti-tumor immunity in small cell lung cancer. Cancer Cell 2020;37:37–54. [PubMed: 31883968]
55. Kieffer Y, Hocine HR, Gentric G, et al. Single-Cell analysis reveals fibroblast clusters linked to immunotherapy resistance in cancer. Cancer Discov 2020;10:1330–51. [PubMed: 32434947]

WHAT IS ALREADY KNOWN ON THIS TOPIC

- Previous studies established the first tumour-based classifications of intrahepatic cholangiocarcinoma (iCCA) that began to unveil a complex desmoplastic tumour microenvironment (TME). By taking into account the previous literature, we aimed to generate a classification able to integrate all elements of the TME.

WHAT THIS STUDY ADDS

- We have identified five novel TME-based classes encompassing both inflamed and non-inflamed profiles. Cross-species analysis between the human disease and the most commonly used animal models identifies high similarity between a *KRAS/p19* murine model and the inflamed *inflammatory stroma* class, while other animal models recapitulate the non-inflamed *hepatic stem-like class. In vivo* drug testing identifies the novel KRAS inhibitor BI3406 plus anti-PD1 therapy as a promising combination strategy in *KRAS*-driven iCCA tumours.

HOW THIS STUDY MIGHT AFFECT RESEARCH, PRACTICE AND/OR POLICY

- The proposed classification provides insights into the rational design of therapeutic strategies targeting both the cancer cells and the surrounding TME. Patients of the *immune classical* class may benefit from immune checkpoint inhibitors as single agents, whereas patients of the *inflammatory stroma* may benefit from immune checkpoint inhibitors in combination with targeted agents (ie, KRAS inhibitors). The implementation of immunotherapy in patients of the non-inflamed classes will require combination therapies tailored to the underlying immune evasion mechanisms and tumour characteristics.

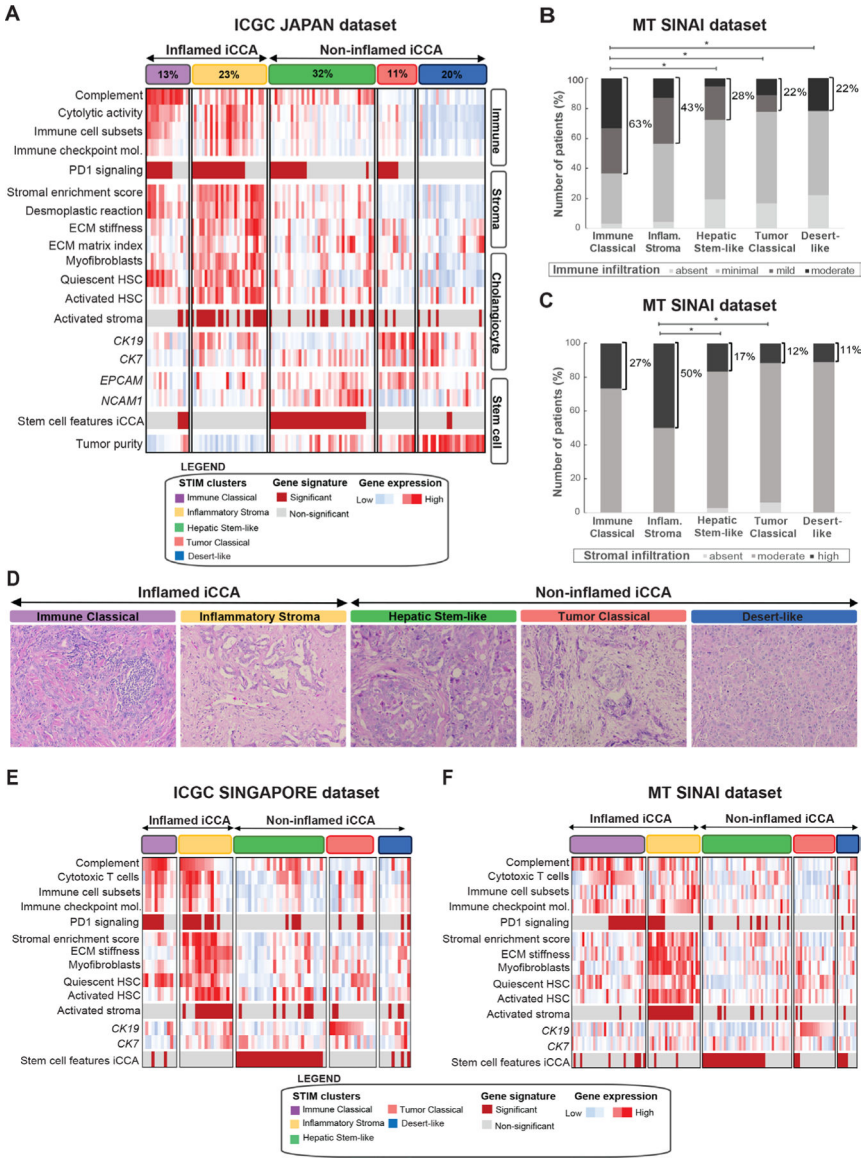

Figure 1.

Identification of the STIM classes of iCCA. (A) Consensus-clustered heatmap in the training dataset (ICGC Japan) using the most representative TME-related components. Semiquantitative evaluation of the immune (B) and stromal infiltration (C) in the STIM classes (*p<0.05). (D) Representative H&E-stained images. Images were captured with ×200. Heatmaps summarise the main features of the STIM classes in the (E) ICGC SINGAPORE and (F) MT SINAI datasets. iCCA, intrahepatic cholangiocarcinoma; STIM, stroma, tumour, immune microenvironment; TME, tumour microenvironment.

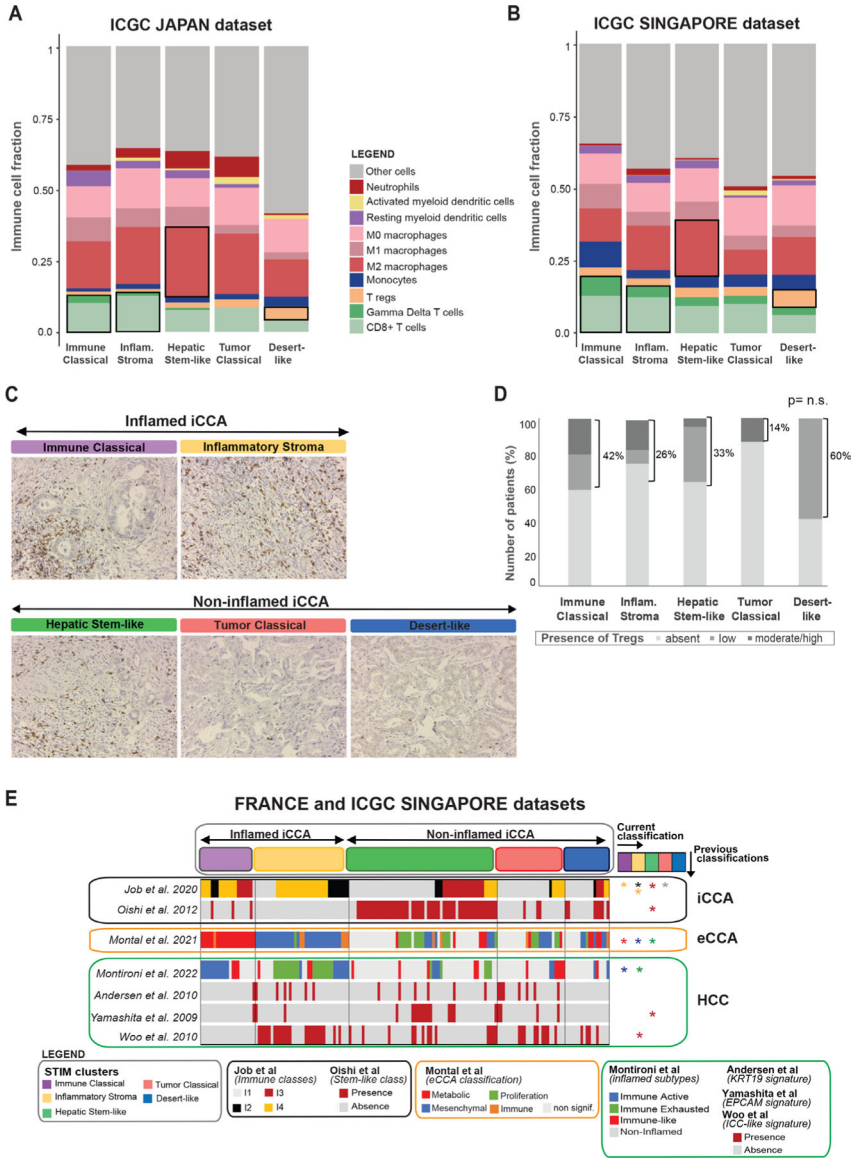

Figure 2.

The STIM classes present different intratumour immune composition. Intratumour immune deconstruction of the STIM classes via CibersortX in the (A) ICGC JAPAN and (B) SINGAPORE cohorts. (C) Representative images of samples of the distinct STIM classes stained with an anti-CD8a antibody. Images were captured with ×200. (D) Quantification of staining intensities for FOXP3 (immune cells only) in the distinct STIM classes. (E) Heatmap representation of the overlap between our STIM classes and previously reported classes of iCCA (first two rows in black rounded rectangle), eCCA (orange rounded rectangle) and HCC (green rounded rectangle). Coloured asterisks on the right indicate significant enrichment in the corresponding class. iCCA, intrahepatic cholangiocarcinoma; eCCA, extrahepatic cholangiocarcinoma; HCC, hepatocellular carcinoma; STIM, stroma, tumour, immune microenvironment.

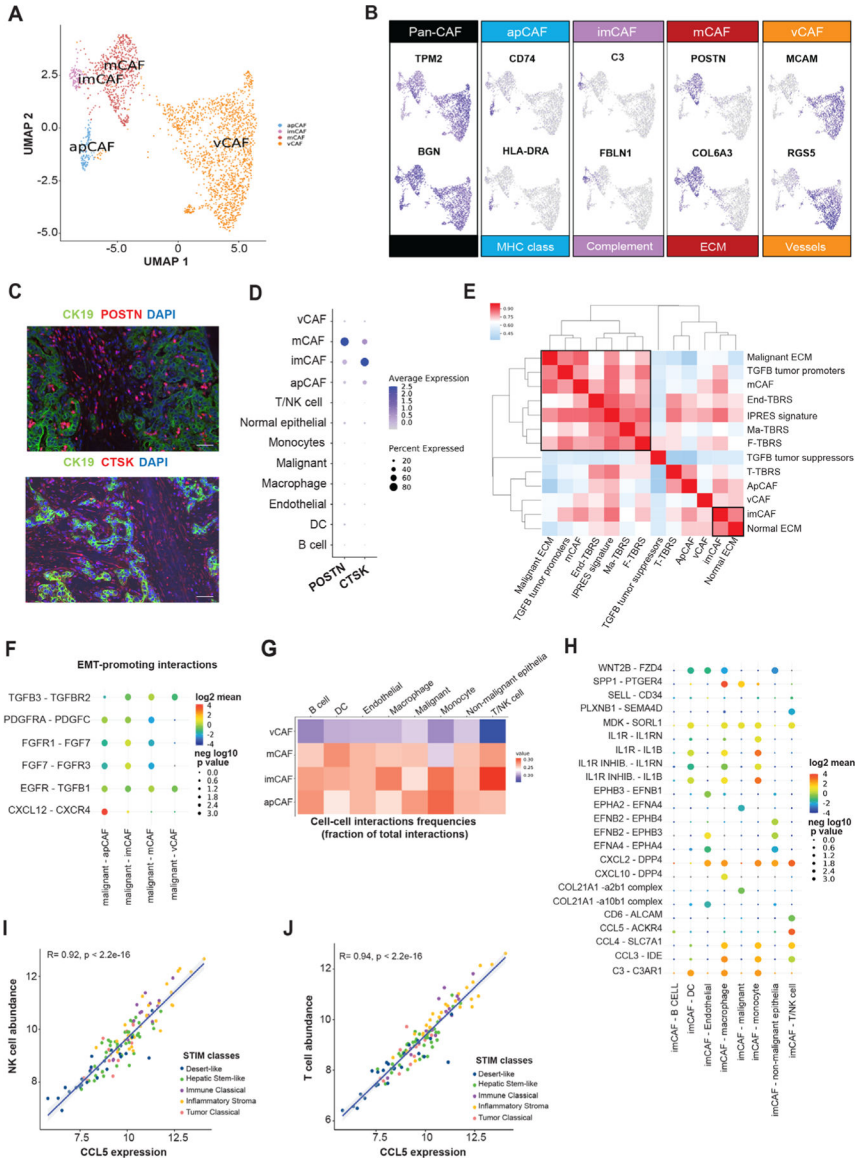

Figure 3.

CAF subtypes represent potential mediators of immune evasion. (A) Colour-coded uMAP representation of the distinct CAF subtypes. (B) tSNE plots colour-coded for the expression of markers genes in each CAF cluster. (C) Immunofluorescence staining for POSTN and CK19 (mCAF) and CTSK and CK19 (imCAF). (D) Dot plot showing expression of *POST* and *CTSK* in the CAF subtypes and other TME cells. (E) Hierarchical clustering of correlation matrix among the distinct CAF signatures, IPRES and ECM and TGFβ related signatures. (F) EMT-related ligand receptors interactions between CAFs and malignant epithelial cells. (G) Heatmap representation of cell–cell interactions frequencies between CAF subtypes and other cells of the TME. (H) Dot plot showing unique receptor–ligand pair interactions inferred between the imCAFs and other cells of the TME. Pearson correlation between CCL5 expression and (I) NK and (J) T cell abundance. ECM, extracellular matrix; TME, tumour microenvironment.

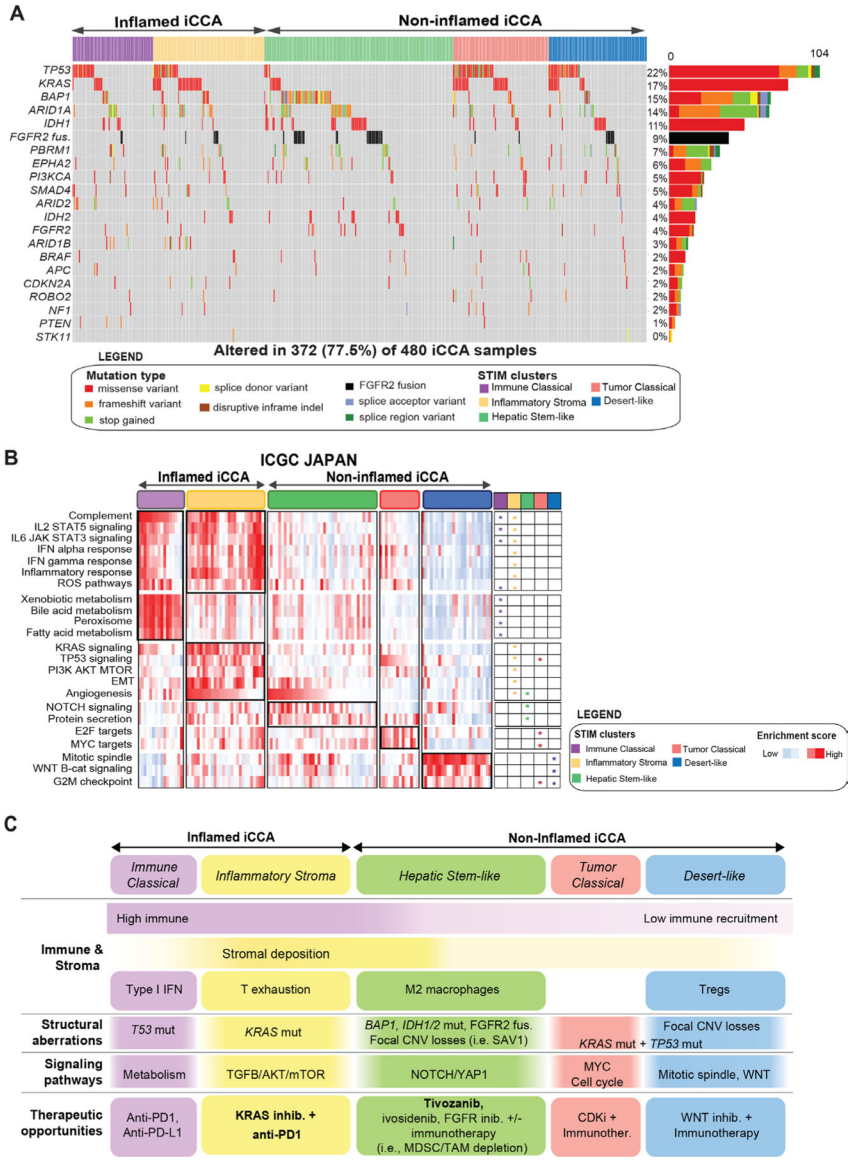

Figure 4.

Association of the STIM classes with mutations and chromosomal instability. (A) Heatmap representation of mutations in driver genes. (B) Heatmap representation of the ssGSEA enrichment score for the Hallmark gene sets in the ICGC JAPAN dataset. (C) The graph summarises the main immune-related, stroma-related and tumour-related features of the five STIM classes. Candidate therapeutic opportunities (bottom row) are recommended based on: (1) preclinical evidence presented in this manuscript (in bold) or (2) molecular and immune characteristics of each class. iCCA, intrahepatic cholangiocarcinoma; STIM, stroma, tumour, immune microenvironment.

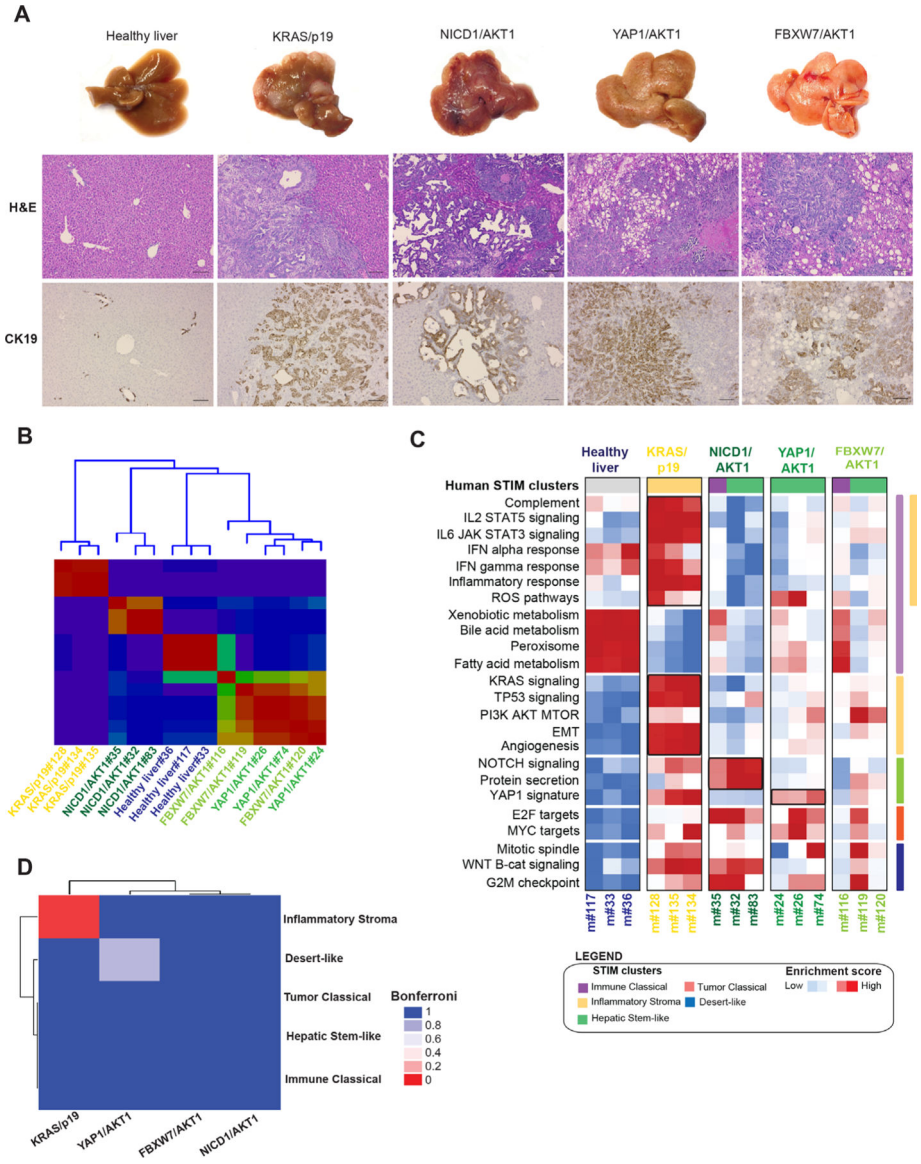

Figure 5.

Available murine models of iCCA recapitulate the *inflammatory stroma* and the *hepatic stem-like* classes. (A) Representative images (H&E and CK19-stained, ×100) of healthy liver and murine iCCA tumours. (B) Unsupervised clustering of RNA-Seq data. (C) Heatmap representation of the ssGSEA enrichment score for the Hallmark pathways. Characteristic pathways of each human class are indicated by a coloured bar on the right of the heatmap. (D) Submap analysis between the human STIM classes and the murine tumours. iCCA, intrahepatic cholangiocarcinoma; STIM, stroma, tumour, immune microenvironment.

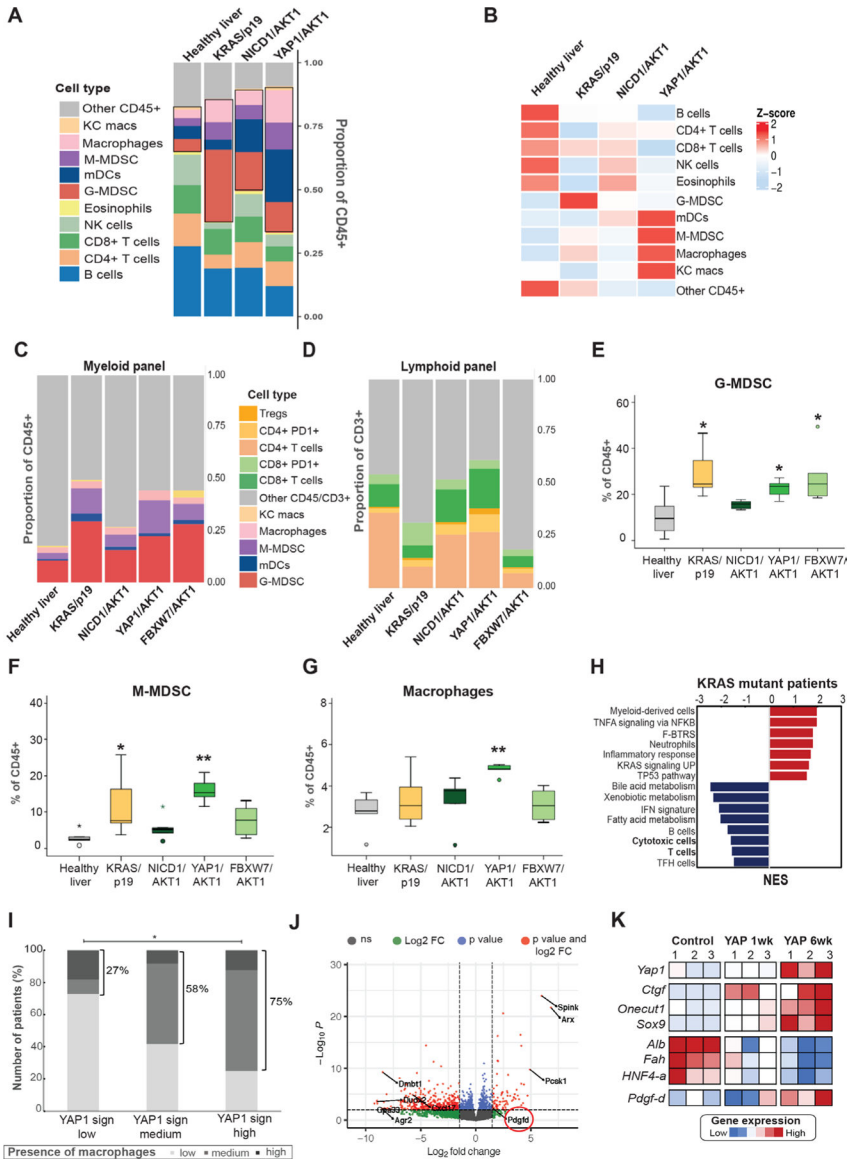

Figure 6.

YAP1 signalling mediates macrophage recruitment. (A) Comparison of lineage proportions between healthy livers and murine tumours (CytOF). (B) Heatmap summarising the average of the percentage of immune cells (Z score) in the total CD45^{+} cells. (C–D) Comparison of lineage proportions between healthy livers and murine tumours (flow cytometry). (E–G) Myeloid populations (percentage of CD45^{+}) in healthy livers and tumours. (H) Top signatures positively (red) or negatively (blue) enriched in human *KRAS*-mutant tumours. (I) Quantification of staining intensities for CD68 in 40 iCCAs. (J) Volcano plots of genes differentially expressed between YAP1/AKT1 and other murine tumours. (K) Heatmap of the expression levels for *Yap1*, *Pdgf-d* and other representative genes in sorted cells on YAP1 activation in tetOYAP mice generated in ref 43. *p<0.05. G-MDSCs, granulocytic myeloid-derived suppressor cells; HSC, hepatic stellate cells; iCCA, intrahepatic cholangiocarcinoma; KC, Kupffer cells; mDCs, myeloid dendritic cells; M-

MDSC, monocytic myeloid-derived suppressor cells; NES, Normalised Enrichment Score; NK, natural killer.

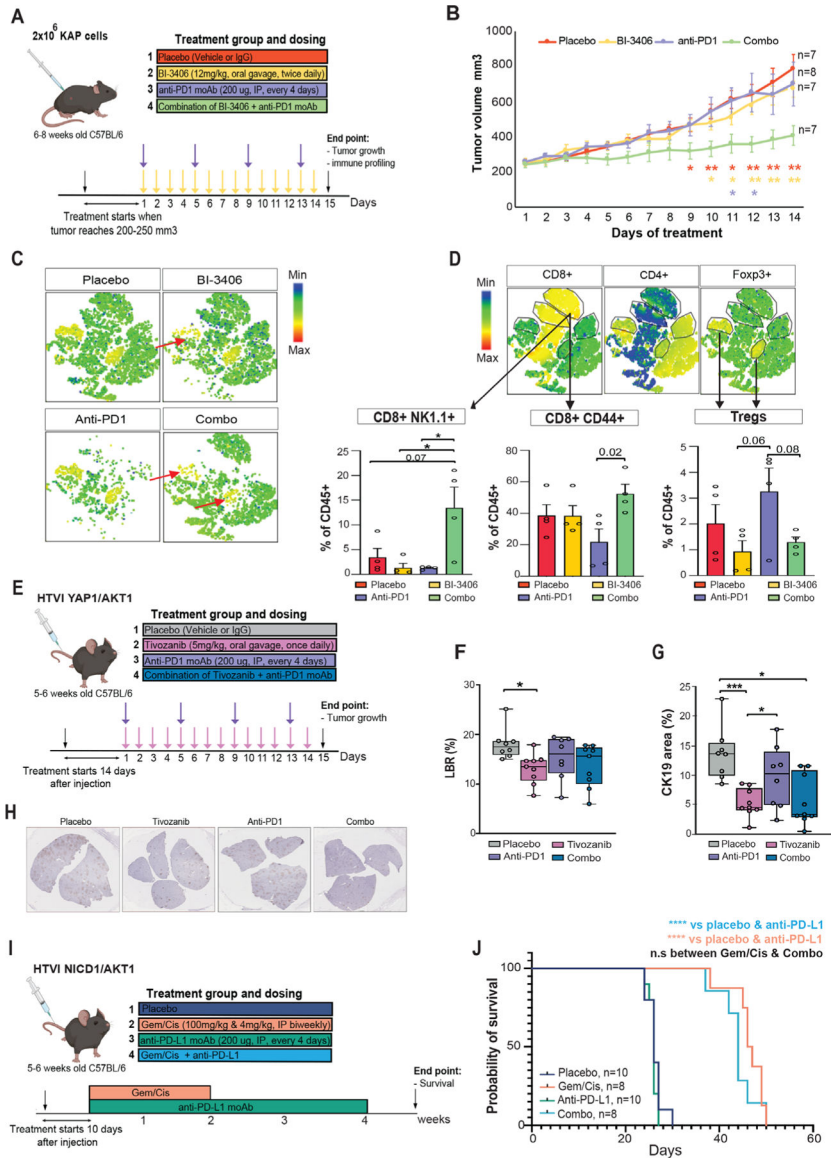

Figure 7.

In vivo antitumoural effect of rationale combination immunotherapies. (A) Experimental treatment scheme in the subcutaneous model with KAP cells (*KRAS* mutant). (B) Tumour growth of mice injected subcutaneously and treated with the KRAS inhibitor BI-3406, anti-PD1 monoclonal antibody (MoAb) or the combination for 14 days. (C) Heatmaps of t-Stochastic neighbour embedding (t-SNE) plot showing expression of $CD45^+$ cells measured by flow cytometry in four mice per each treatment arm. (D) Heatmaps of t-SNE plot showing expression of thrree selected markers (CD8+, CD4+, Foxp3+, top panel) uncover immune cell changes induced by single agents versus combo; scale is indicated. Bottom panel: percentage of proliferating $CD8^+$ cells ($CD8^+NK1.1^+$ panel), memory CD8+ ($CD8^+CD44^+$ panel) and Tregs (bottom right) in the four treatment arms (n=4 mice/arm); bars indicate SE. (E) Experimental treatment scheme in the HTVI model YAP1/AKT1. (F) Liver body ratio (LBR) of mice injected with YAP1 and AKT1 plasmids and treated

with tivozanib, anti-PD1 moAb or combination. (G) Quantification of CK19 stained area as readout of tumorous growth in mice enrolled in one of the four arms. *<0.05; **<0.01; ***<0.001. (H). Representative images of liver from mice treated with placebo, tivozanib, anti-PD1 or combo (scans at 20×). (I) Experimental treatment scheme in the HTVI model NICD1/AKT1. (J) Survival curves of the four treatment arms. *<0.05; **<0.01; ***<0.001; ****<0.0001; n.s., non-significant. Tregs, regulatory T cells.